

Multi-Wave band Synchrotron Polarization of Gamma-Ray Burst Afterglows

JIRO SHIMODA^{1,2,3} AND KENJI TOMA^{1,2}

¹*Frontier Research Institute for Interdisciplinary Sciences, Tohoku University, Sendai 980-8578, Japan*

²*Astronomical Institute, Graduate School of Science, Tohoku University, Sendai 980-8578, Japan*

³*Department of Physics, Graduate School of Science, Nagoya University,
Furo-cho, Chikusa-ku, Nagoya 464-8602, Japan*

(Received today)

Submitted to ApJ

ABSTRACT

Multi-wave band synchrotron linear polarization of gamma-ray burst (GRB) afterglows is studied under the assumption of an anisotropic turbulent magnetic field with a coherence length of the plasma skin-depth scale in the downstream of forward shocks. We find that for typical GRBs, in comparison to the optical polarization, the degree of radio polarization shows a similar temporal evolution but a significantly smaller peak value. This results from differences in observed intensity image shapes between the radio and optical bands. We also show that the degree of the polarization spectrum undergoes a gradual variation from the low- to the high-polarization regime above the intensity of the spectral peak frequency, and that the difference in polarization angles in the two regimes is zero or 90 degrees. Thus, simultaneous multi-wave band polarimetric observations of GRB afterglows would be a new determinative test of the plasma-scale magnetic field model. We also discuss theoretical implications from the recent detection of radio linear polarization in GRB 171205A with ALMA and other models of magnetic field configuration.

Keywords: gamma-ray burst: general — magnetic fields — shock waves — polarization — gamma-ray burst: individual (GRB 171205A)

1. INTRODUCTION

Gamma-ray bursts (GRBs) are the brightest transients in the gamma-ray sky. The progenitor of some long-duration GRBs was established as the core collapse of massive stars (Hjorth & Bloom 2012, and references therein), and that of one short-duration GRB as coalescence of a double neutron star binary (Abbott et al. 2017). Extensive efforts in lightcurve and spectral observations of GRBs and theoretical arguments led to the standard scenario: The progenitor system gives rise to a new-born black hole with an accretion disk, and drives a relativistic jet, which emits prompt gamma-rays. Then the interaction of the jet with the circumburst medium generates a reverse shock and a forward shock, which emit long-lived afterglows observed in the wave bands

from radio to gamma-rays. In particular, synchrotron emission of nonthermal electrons created by the forward shocks can explain the observational results of many late-phase afterglows (Mészáros 2002; Piran 2004; Kumar & Zhang 2015, for reviews).

Several major problems remain concerning the standard scenario, however, which include the origins of the strong magnetic field and the nonthermal electrons in the shocked region (Sironi et al. 2015, for a review). Relativistic collisionless shocks are formed with amplification of the magnetic field on the plasma skin-depth scale by Weibel instability, although whether the amplified magnetic field can be maintained at a sufficiently long distance in the downstream of a shock (Medvedev & Loeb 1999; Gruzinov & Waxman 1999; Keshet et al. 2009; Sironi & Spitkovsky 2011; Asano et al. 2020) is a subject of debate. Other mechanisms of field amplification on larger scales have also been investigated (Sironi & Goodman 2007; Inoue et al. 2013b; Duffell & MacFadyen 2014; Tomita et al. 2019).

Particle-in-cell simulations of relativistic shocks show nonthermal electron production (Sironi et al. 2013), but the physical mechanism of electron acceleration is still elusive since the electron spectral index and maximum energy depend on the unknown magnetic field properties. Furthermore, the number ratio of nonthermal to thermal electrons has not been probed by observations yet (Toma et al. 2008), and this affects the estimate of the total energies of GRBs (Eichler & Waxman 2005), which then affects the estimate of the detectability of GRBs’ multi-messenger and high-redshift signals (Murase et al. 2006; Kimura et al. 2017; Inoue et al. 2013a; Toma et al. 2016).

Polarimetric observations in addition to the light-curve and spectral ones are powerful for solving such problems on collisionless shock physics (for reviews Lazzati 2006; Toma 2013; Covino & Gotz 2016). During the last decade, polarimetric observations have achieved a number of new measurements and indications; in gamma-ray prompt emission with GAP (Yonetoku et al. 2011, 2012), INTEGRAL (Götz et al. 2009, 2013), AstroSat (Sharma et al. 2019) and POLAR (Zhang et al. 2019; Kole 2019; Burgess et al. 2019),¹ in optical prompt emission and early afterglows with the Liverpool Telescope (Mundell et al. 2013; Kopač et al. 2015; Steele et al. 2017; Jordana-Mitjans et al. 2020), the Kanata Telescope (Uehara et al. 2012), and Master Telescopes (Troja et al. 2017), and in radio afterglows with the ALMA (Urata et al. 2019; Laskar et al. 2019). Circular polarization has also been detected in the optical band (Wiersema et al. 2014).

The radio polarization had not been detected until very recently, probably because the observed spectral parts ($\simeq 8.4$ GHz with the VLA in most cases) were optically thick due to synchrotron self-absorption (Taylor et al. 2005; Granot & Taylor 2005; Granot & van der Horst 2014; van der Horst et al. 2014). The recent two detections were performed for optically thin parts at the higher frequency with ALMA, $\simeq 97.5$ GHz. One of them revealed that the polarization degree (PD) in the forward shock afterglow of GRB 171205A, $\Pi \simeq 0.27\% \pm$

0.04% (Urata et al. 2019)², is significantly lower than the typical late-phase optical afterglow PD, $\Pi \sim 1 - 3\%$ (Covino et al. 2004; Covino & Gotz 2016; Urata et al. 2019; Stringer & Lazzati 2020).

The difference between the optical and radio polarizations was theoretically discussed by focusing on the Faraday rotation effect by thermal electrons or radiatively-cooled electrons in the shocked region with large-scale magnetic turbulence (Matsumiya & Ioka 2003; Sagiv et al. 2004; Toma et al. 2008). For the anisotropic turbulent magnetic field with a coherence length on the plasma skin-depth scale (Medvedev & Loeb 1999; Sari 1999; Ghisellini & Lazzati 1999; Rossi et al. 2004; Gill & Granot 2020), the Faraday rotation effects are tiny, and little attention has been paid to the wavelength dependence of polarization (but see Mao & Wang 2017). Only Rossi et al. (2004) showed a calculation result in the plasma-scale turbulent field model with PD at the observed frequency of $\nu \ll \nu_m$ (which they refer to as the ‘radio branch’) is lower than that at $\nu \gg \nu_m$ (‘optical branch’), where ν_m is the spectral peak frequency of afterglow synchrotron emission. However, they did not clarify the physical reason for this result nor did they mention on how PD varies around $\nu \sim \nu_m$, for which ALMA polarimetric observations will be often performed, as suggested by GRB 171205A (Urata et al. 2019).

In this paper, we calculate the PD temporal variations of GRB afterglows at multiple wave bands in the anisotropic plasma-scale turbulent magnetic field model, and pin down the physical reason for the wavelength dependence of PD by showing the relationship of the afterglow image on the sky with the net PD when observed as a point source. Furthermore, we derive PD spectra, in which we find gradual PD variations above $\nu \sim \nu_m$, and show their parameter dependence. These analyses will be crucial for testing the plasma-scale magnetic field model with polarimetric data at ALMA bands (and simultaneous optical polarimetric data) and be useful for theoretical prediction of radio polarization for different magnetic field models.

This paper is organized as follows. In Section 2, we introduce a standard model of the dynamics and emission fluxes of the expanding forward shocks. Then, in Section 3, we consider synchrotron emission and its po-

¹ Reports of gamma-ray polarization measurements include those of GRB 021206 by RHESSI (Coburn & Boggs 2003) which were refuted by Rutledge & Fox (2004) and Wigger et al. (2004) and those of GRB 041219A by INTEGRAL SPI (Kalemci et al. 2007) were inconsistent with the same event data by INTEGRAL IBIS (Götz et al. 2009). We should note that even for the recent measurements their detection significances are mostly $\sim 3\sigma$.

² This detection is now under debate. Laskar et al. (2020) claimed that the systematic error of polarimetric calibration is $\sim 0.1\%$, which is more than three times larger than the value in the ALMA technical handbook, and then inferred a 3σ upper limit $\Pi < 0.30\%$.

larization with an assumption of an anisotropic plasma-scale turbulent magnetic field. After explaining the parameter sets that we use in Section 4, we show the calculation results of multi-wave band synchrotron polarization and their physical interpretation in Section 5. Section 6 is devoted to a summary of our findings and a discussion.

2. BLAST WAVE DYNAMICS AND EMISSION FLUX

We consider GRB afterglows as synchrotron emission from relativistically expanding spherical blast waves, and calculate their dynamics and emission fluxes by following the formulation of [Granot et al. \(1999a\)](#) and taking into account of the collimation of outflows. The radius of the shock front is $R = R(t)$ and its Lorentz factor Γ is proportional to $R^{-3/2}$ (adiabatic expansion, i.e., constant explosion energy). The internal structure of the shocked region with $\Gamma \gg 1$ is given by (cf. [Blandford & McKee 1976](#), eqs. 28-30 and 40-42)

$$n' = 4\gamma_f n_0 \chi^{-\frac{5}{4}}, \quad (1)$$

$$\gamma = \gamma_f \chi^{-\frac{1}{2}}, \quad (2)$$

$$e' = 4n_0 m_p c^2 \gamma_f^2 \chi^{-\frac{17}{12}}, \quad (3)$$

where the superscript prime denotes a value measured in the rest frame of the fluid, n is the number density, γ is the Lorentz factor of the fluid, and e is the internal energy, respectively. $\gamma_f \simeq \Gamma/\sqrt{2}$ indicates the Lorentz factor of the fluid just behind the shock. The ambient number density measured in the observer frame is n_0 . The speed of light and proton mass are c and m_p , respectively. The self-similar variable χ is defined as

$$\chi = 1 + 16\gamma_f^2 \left(\frac{R-r}{R} \right). \quad (4)$$

Note that the shocked region may have a thickness of $\Delta \sim R/4\gamma^2$. The radius R can be rewritten as function of a photon arrival time to the observer, T . We use a spherical coordinate system centered on the blast wave and set our line of sight along the z -axis for convenience. For a photon emitted at time t and position (r, μ) in the observer frame, where $\mu \equiv \cos \theta$, the arrival time is

$$T_z = \frac{T}{1+z} = t - \frac{r\mu}{c}, \quad (5)$$

where z is the cosmological redshift and we choose that $T = 0$ as the arrival time of a photon emitted from the origin at time $t = 0$. Solving the motion equation of the shock, $dR/cdt = \sqrt{1-1/\Gamma^2}$ with $\Gamma \propto R^{-3/2}$ and $\Gamma \gg 1$, we obtain

$$R \simeq \frac{cT_z}{1-\mu+1/(8\Gamma^2)}. \quad (6)$$

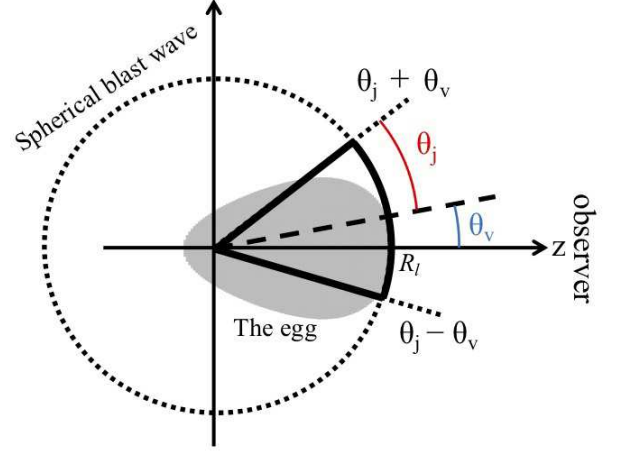


Figure 1. Schematic diagram of a collimated blast wave. The dotted curve corresponds to the shock surface of a spherical blast wave, which expands radially. We only consider the part of the blast wave within the angle interval $2\theta_j$ (thick solid line) as produced by a GRB jet. Our line of sight is fixed along the z -axis, which makes an angle θ_v with the jet axis (dashed line). For the spherical blast wave, photons from the shaded region (egg) have the same arrival time T . The collimated region of the egg is also described by Figure 7, in which the white (black) line indicates $\theta = \theta_j - \theta_v$ ($\theta = \theta_j + \theta_v$) for $\phi = 0$ and π .

The surface described by $R = R(\mu, T)$ at which the photons have the same arrival time forms an elongated ‘egg’ shape that is no longer spherically symmetric, as illustrated in Figure 1. Such a relativistic lookback geometry was first introduced for constant Γ by [Rees \(1966\)](#). Equation (6) is a version of the geometry for $\Gamma \propto R^{-3/2}$. We will refer to this surface as ‘the egg’ (cf. [Granot et al. 1999a](#)). χ is now a self-similar variable dependent on T , r , and μ .

It is useful to additionally introduce another self-similar variable,

$$y = \frac{R}{R_l}, \quad (7)$$

where R_l is the semi-major axis of the egg. Then we can describe the condition of adiabatic expansion as

$$\gamma_f = \gamma_l y^{-\frac{3}{2}}, \quad (8)$$

where γ_l is the Lorentz factor of the fluid just behind the shock at the semi-major axis of the egg. From Eq. (5), we find that relationships between the variables (r, μ) and (χ, y) are

$$r \simeq R_l y, \quad \mu \simeq 1 - \frac{1-\chi y^4}{16\gamma_l^2 y}. \quad (9)$$

Note that the position $(\chi, y) = (1, 1)$ presents $(r, \mu) = (R_l, 1)$, and $R_l = 8\Gamma^2 cT_z = 16\gamma_l^2 cT_z$.

Figure 1 schematically shows the geometry of our system. We regard a part of the blast wave within the angle interval $2\theta_j$ as produced by a GRB jet, and exclude the other part. The viewing angle θ_v is defined as the angle between the jet axis and our line of sight (z -axis). The position $\hat{\mathbf{r}} = (\sin\theta \cos\phi, \sin\theta \sin\phi, \cos\theta)$ on the jetted region satisfies the condition $\hat{\mathbf{r}} \cdot \mathbf{n}_j \geq \cos\theta_j$, where $\mathbf{n}_j = (\sin\theta_v, 0, \cos\theta_v)$ is the direction of the vector along the jet axis. This condition is rewritten as

$$\cos\phi \geq \frac{\cos\theta_j - \cos\theta_v \cos\theta}{\sin\theta_v \sin\theta} \equiv \cos\phi_{\text{ec}}, \quad (10)$$

and this leads to the egg missing part.

The energy flux density of synchrotron emission should be considered based on this egg. Granot et al. (1999a) provided a general formula of the flux density of radiation from a spherical expanding system for the case of an optically thin limit and an isotropic radiation measured in the fluid frame,

$$F(\nu, T) = \frac{1+z}{4\pi d_L^2} \int_0^{2\pi} d\phi \int_{-1}^1 d\mu \int_0^\infty r^2 dr \times \frac{P'(\nu', \mathbf{r}, T_z + r\mu/c)}{\gamma^2 (1 - \beta\mu)^2}, \quad (11)$$

where d_L is the luminosity distance to the GRB, $\beta = \sqrt{1 - 1/\gamma^2}$, and $\nu' = \gamma\nu(1 - \beta\mu)$ is the frequency of photon measured in the fluid frame, respectively. The factor $1/\gamma^2(1 - \beta\mu)^2$ represents the Doppler beaming effect, by which the bright region is concentrated to $\theta \lesssim \gamma^{-1}$. The emission from the region at $\theta > \gamma^{-1}$ is beamed away from the line of sight. The emission power P' depends on ϕ in our jet model: $P' = 0$ at which the inequality of Eq. (10) is not satisfied. Using the self-similar variables χ and y , we obtain

$$F = \frac{4R_l^3(1+z)}{\pi d_L^2} \int_0^{2\pi} d\phi \int_1^{\chi_{\text{max}}} d\chi \int_0^{\chi^{-\frac{1}{4}}} dy \frac{\chi y^{10} P'}{(1 + 7\chi y^4)^2}. \quad (12)$$

We take $\chi_{\text{max}} = 1 + 16\gamma_f^2$.

The surface brightness profile (i.e. intensity image on the sky) at a given arrival time T is also derived. Let R_\perp be a distance of a position on the sky from the line of sight axis,

$$R_\perp \equiv r \sin\theta \simeq R_l y \sqrt{1 - \mu^2} \simeq \frac{\sqrt{2}R_l}{4\gamma_l} \sqrt{y - \chi y^5}. \quad (13)$$

The maximum value of the distance is given on the surface of the egg at which $(\chi, y) = (1, 5^{-\frac{1}{4}})$ as $R_{\perp, \text{max}} \simeq$

$0.26R_l/\gamma_l$. Its angular size is $R_{\perp, \text{max}}/(5^{-\frac{1}{4}}R_l) \sim 0.4\gamma_l^{-1}$. Thus, the emission from the whole egg is bright due to the Doppler beaming.

Since the entire size of the intensity image becomes larger with time due to the expansion of the blast wave and its deceleration, it is convenient to introduce a variable of $x \equiv R_\perp/R_{\perp, \text{max}}$. The differential area of the image can be written as

$$dS_\perp = R_\perp dR_\perp d\phi = R_{\perp, \text{max}}^2 x dx d\phi. \quad (14)$$

Thus, we obtain the flux density element in the image as

$$\begin{aligned} \frac{dF}{dS_\perp} &= \frac{4}{\pi} \left(\frac{R_l}{d_L} \right)^2 \frac{(1+z)^2}{cT} \frac{\chi y^5 P'}{(1 + 7\chi y^4)^2} dy \\ &= \frac{4}{\pi} \left(\frac{R_l}{d_L} \right)^2 \frac{(1+z)^2 y^2 (y - ax^2) P'}{(8y - 7ax^2)^2} dy, \end{aligned} \quad (15)$$

where $a = 8(\gamma_l R_{\perp, \text{max}}/R_l)^2$ and we use $\chi = y^{-4} - ax^2 y^{-5}$. The surface brightness profile is obtained after the y integration as function of R_\perp and ϕ . The range of the y integration is determined by the condition $\chi > 1$. Note that the ϕ dependence of P' (Equation 10) can make the intensity image asymmetric (see Figure 1 and 2).

3. SYNCHROTRON POWER AND POLARIZATION

To calculate the synchrotron power at each point, we assume that the energies of electrons e'_e and magnetic field e'_B are fixed fractions of the local internal energy; $e'_e = \epsilon_e e'$ and $e'_B = \epsilon_B e'$. We suppose that the electrons are accelerated by the forward shock and have a single power-law distribution function everywhere:

$$N(\gamma_e) = K \gamma_e^{-p} \quad \text{for } \gamma_e \geq \gamma_m, \quad (16)$$

where γ_e is electron's Lorentz factor. The normalization constant K and minimum Lorentz factor of electrons γ_m are determined as

$$K = (p-1)n'\gamma_m^{p-1}, \quad (17)$$

and

$$\gamma_m = \left(\frac{p-2}{p-1} \right) \frac{\epsilon_e e'}{n' m_e c^2}, \quad (18)$$

respectively. Granot et al. (1999a) gives approximate synchrotron power formulas,

$$P' = \begin{cases} P'_{\nu, \text{max}} \left(\frac{\nu'}{\nu'_m} \right)^{\frac{1}{3}} & \text{for } \nu' < \nu'_m \\ P'_{\nu, \text{max}} \left(\frac{\nu'}{\nu'_m} \right)^{-\frac{p-1}{2}} & \text{for } \nu' > \nu'_m \end{cases}, \quad (19)$$

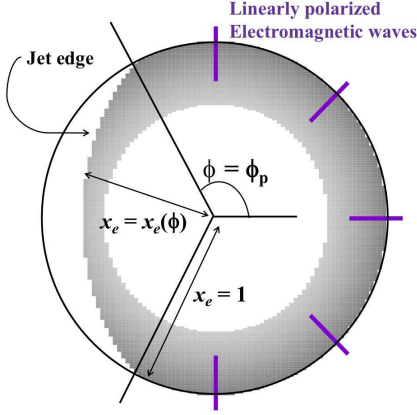


Figure 2. Schematic picture of the asymmetry of the intensity image and the distribution of local PAs. ϕ_p denotes the azimuthal angle of the region, which does not have a part missing due to the finite extent of the jet. The angular distance from the line-of-sight axis to the outer edge of nonzero intensity is denoted by x_e .

where

$$P'_{\nu, \max} = 0.88 \frac{4(p-1)}{3p-1} \frac{n' P'_{e, \text{av}}}{\nu'_{\text{syn}} \langle \gamma_e \rangle}. \quad (20)$$

Here, $P'_{e, \text{av}}$ is the synchrotron power by a single electron with an average Lorentz factor of $\langle \gamma_e \rangle \equiv \epsilon_e e' / (n' m_e c^2)$,

$$P'_{e, \text{av}} = \frac{4}{3} \sigma_T c \beta_e^2 \langle \gamma_e \rangle^2 \epsilon_B e', \quad (21)$$

where σ_T is the Thomson cross section, and $\beta_e = \sqrt{1 - 1/\langle \gamma_e \rangle^2}$, respectively. The synchrotron peak frequency measured in the fluid frame is

$$\nu'_{\text{syn}}(\gamma_e) = \frac{3\gamma_e^2 q_e B'}{16m_e c}, \quad (22)$$

where q_e is the electron's electric charge and $B' = \sqrt{8\pi\epsilon_B e'}$ is the local magnetic field strength. We define $\nu'_m = \nu'_{\text{syn}}(\gamma_m)$. In this paper, we use this approximate power and fix the power-law index of electron's energy spectrum to be $p = 3$ for simplicity.

Synchrotron polarization depends on the magnetic field configuration at each position. In this paper, we focus on the model in which the magnetic field is turbulent with coherence length on the plasma scale, i.e., the power spectrum of magnetic turbulence ranges only around the proton skin-depth scale, as done in Sari (1999) and Ghisellini & Lazzati (1999). Linear analysis and particle-in-cell simulations of relativistic collisionless shocks show that the plasma-scale field perpendicular to the shock normal \mathbf{B}'_{\perp} is predominantly generated by Weibel instability at the shock (Medvedev & Loeb 1999; Gruzinov & Waxman 1999). The nonlinear evolution of the field structure in the downstream of the shock

is not fully understood, but the direction of the distribution of the field may be anisotropic (Nishikawa et al. 2003; Kato 2005; Spitkovsky 2008; Keshet et al. 2009; Sironi et al. 2015). We parameterize its degree of anisotropy as $\xi^2 \equiv 2\langle B'^2_{\parallel} \rangle / \langle B'^2_{\perp} \rangle$.

Particle-in-cell simulations also show that nonthermal electron acceleration is efficient in the plasma-scale field induced by Weibel instability when the unshocked medium is not or weakly magnetized (Sironi & Spitkovsky 2011; Sironi et al. 2013). For this reason we neglect an ordered magnetic field in our calculations. The strong helical magnetic field possibly inside the jet cannot be advected through the contact discontinuity and thus cannot affect the forward shock.

Here, we derive the Stokes parameters of emission at each position, $\langle i' \rangle, \langle q' \rangle, \langle u' \rangle$, averaged due to contributions from magnetic fields oriented differently, by following Sari (1999) (see also Toma et al. 2009; Lan et al. 2018). Let us consider that a right-handed coordinate system $x'y'z'$ whose axis z' is along the photon wavevector \mathbf{k}' , and the direction of \mathbf{B}' is described by spherical coordinates (θ'_B, ϕ'_B) . Then the synchrotron intensity depends on θ'_B as $i' \propto \sin^{\epsilon} \theta'_B$, where $\epsilon = (p+1)/2$. The direction of the polarization is perpendicular to both \mathbf{k}' and \mathbf{B}' , so that

$$q' = -i' f \cos 2\phi'_B, \quad u' = -i' f \sin 2\phi'_B, \quad (23)$$

where $f = (p+1)/(p+7/3)$ (Rybicki & Lightman 1979). For another right-handed coordinate system of $1'2'3'$ whose axis of $3'$ is along the shock normal and on the plane $x'z'$, we describe the direction of \mathbf{B}' by spherical coordinates (α', η') . In the case of an anisotropic magnetic field that has symmetry on the plane $1'2'$, we can define a probability per unit of solid angle for the field to have the polar angle α' , $F_B(\alpha')$, and allow the field strength to depend on α' , $B' = B'(\alpha')$ (Sari 1999; Gill & Granot 2020). Recalling that the angle between axes z' and $3'$ corresponds to the viewing angle θ' , we have the relations

$$\begin{aligned} \sin \theta'_B \cos \phi'_B &= \sin \alpha' \cos \eta' \cos \theta' - \cos \alpha' \sin \theta' \\ \sin \theta'_B \sin \phi'_B &= \sin \alpha' \sin \eta' \\ \cos \theta'_B &= \sin \alpha' \cos \eta' \sin \theta' + \cos \alpha' \cos \theta' \end{aligned} \quad (24)$$

Averaging i', q', u' with respect to the field distribution leads to $\langle u' \rangle = 0$ due to the symmetry on the plane of $1'2'$ and gives the local PD as

$$\begin{aligned} \langle f \rangle &= \frac{\langle |q'| \rangle}{\langle i' \rangle} \\ &= \frac{|\int (-f \cos 2\phi'_B) [B'(\alpha') \sin \theta'_B]^{\epsilon} F_B(\alpha') \sin \alpha' d\alpha' d\eta'|}{\int [B'(\alpha') \sin \theta'_B]^{\epsilon} F_B(\alpha') \sin \alpha' d\alpha' d\eta'}. \end{aligned} \quad (25)$$

For the case of $p = 3$ ($\nu' > \nu'_m$), one has $\langle f \rangle$ without specifying the functional forms of $F_B(\alpha')$ and $B'(\alpha')$,

$$\langle f \rangle = \frac{|\xi^2 - 1| \sin^2 \theta'}{2 + (\xi^2 - 1) \sin^2 \theta'}. \quad (26)$$

For $\nu' < \nu'_m$, we may adopt a model of the field distribution given by Sari (1999),

$$B'(\alpha') \propto (\xi^2 \sin^2 \alpha' + \cos^2 \alpha')^{-1/2}, \quad F_B(\alpha') \propto B'^3(\alpha'). \quad (27)$$

In this model, the distribution of $B'(\alpha')$ shapes an ellipsoid with aspect ratio ξ , and $2\langle B_{\parallel}^2 \rangle / \langle B_{\perp}^2 \rangle = \xi^2$ is consistently obtained (Gill & Granot 2020). For an extreme case of $\xi^2 = 0$, i.e., $\mathbf{B}' = \mathbf{B}'_{\perp}$, we have $\langle f \rangle$ by setting $B'(\alpha') = \text{const.}$ and $F_B(\alpha') = \delta(\alpha' - \pi/2)$ in Equation (25). The calculation results of $\langle f \rangle$ for $\nu' > \nu'_m$ and $\nu' < \nu'_m$ are shown in Figure 3. The solid and dashed lines represent $\xi^2 = 0$ and $\xi^2 = 0.72$, respectively. We will show the calculation results of polarization mainly for $\xi^2 = 0$, and also show in Section 5.5 that the typical PD measured in the late-phase optical afterglows of $\sim 1 - 3\%$ is reproduced with $\xi^2 = 0.72$ in the case of $\theta_v = \theta_j/2$.

For $\xi^2 < 1$ we obtain $\langle q' \rangle > 0$. This means that the direction of polarization is along axis x' , which lies on the plane including \mathbf{k}' and the shock normal. The Lorentz transformation of radiation (i.e., the Doppler beaming) does not change this configuration, i.e., the direction of the polarization in the observer frame lies on the plane including \mathbf{k} and the shock normal. As a result, the observed polarization angle (PA) at the local point on the sky is identical to ϕ (see Figure 2).

We obtain the surface brightness by the y integration obtain the surface brightness by the y integration,

$$S_I = \int \frac{dF}{dS_{\perp} dy} \langle \sin^{\epsilon} \theta'_B \rangle dy, \quad (28)$$

$$S_Q = \int \langle f \rangle \frac{dF}{dS_{\perp} dy} \langle \sin^{\epsilon} \theta'_B \rangle dy \cos 2\phi, \quad (29)$$

$$S_U = \int \langle f \rangle \frac{dF}{dS_{\perp} dy} \langle \sin^{\epsilon} \theta'_B \rangle dy \sin 2\phi. \quad (30)$$

In summary, the synchrotron emission at each position is polarized due to the anisotropy of turbulent magnetic field even though its coherence length is on the plasma skin-depth scale, many orders of magnitude smaller than the hydrodynamic scale, and the PA is identical to ϕ (see Figure 2). The combination of the relativistic aberration (or Doppler beaming) and off-axis viewing of the jet ($\theta_v \neq 0$) leads to an asymmetry in the observed image as explained in Section 2. Therefore, the emission integrated over the image can have net PD.

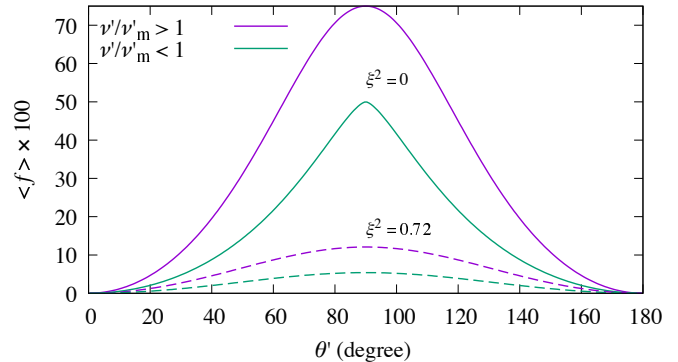


Figure 3. The local PDs $\langle f \rangle$ as functions of θ' for $\nu'/\nu'_m > 1$ (purple) and $\nu'/\nu'_m < 1$ (green). The solid and dashed lines represent $\xi^2 = 0$ and $\xi^2 = 0.72$, respectively. Note that for $\gamma = 10$ as an example, the angular scales of the Doppler-beamed region $\theta = 1/\gamma$ and the whole emission region $\theta_j + \theta_v = 9$ degree (as given in Section 5) correspond to $\theta' \simeq 90$ degree and $\simeq 115$ degree, respectively.

4. PARAMETER SETTING

We perform calculations of PD temporal variations (which we call PD curves hereafter) and PD spectra of GRB afterglows by using the above formulae with fixed parameters of the isotropic energy of blast wave $E_{\text{iso}} = 10^{52}$ erg, $n_0 = 1 \text{ cm}^{-3}$, $\epsilon_e = 0.1$, $\epsilon_B = 0.01$, and $\theta_j = 6$ degree. They are typical parameter values for long GRBs (e.g., Panaitescu & Kumar 2002). We assume nearby events with $z \sim 0$. The sideways expansion of collimated relativistic blast waves is considered to be weak, as indicated by high-resolution hydrodynamic simulations (Zhang & MacFadyen 2009; van Eerten & MacFadyen 2012), so that we set $\theta_j = \text{const.}$, for simplicity. The Lorentz factor of the blast wave is given by

$$\Gamma = \frac{1}{2} \left(\frac{17E_{\text{iso}}}{16\pi n_0 m_p c^5 T_z^3} \right)^{\frac{1}{8}}. \quad (31)$$

Then, for a given θ_v , we obtain observed synchrotron flux and polarization as functions of ν and T .

The magnetic field strength, proton plasma frequency, and electron cyclotron frequency measured in the fluid frame are estimated as $B' = \sqrt{8\pi\epsilon_B e'} \simeq 0.1 y^{-3/2} \chi^{-17/24} (T/1 \text{ day})^{-3/8}$ G, $\omega'_{\text{pp}} = \sqrt{4\pi q_p^2 n' / \langle \gamma_p \rangle m_p} \simeq 3 \times 10^3 \chi^{-13/24}$ Hz, and $\omega'_{\text{ce}} = q_e B' / m_e c \simeq 2 \times 10^6 y^{-3/2} \chi^{-17/24} (T/1 \text{ day})^{-3/8}$ Hz, where q_p is the proton's electric charge, and $\langle \gamma_p \rangle = e' / n' m_p c^2$ is the average Lorentz factor of thermal protons. The coherence length of turbulent magnetic field induced by Weibel instability is on the plasma skin-depth scale, $c/\omega_{\text{pp}} \sim 10^7 \chi^{13/24}$ cm, which is sufficiently small compared to the size of emission region,

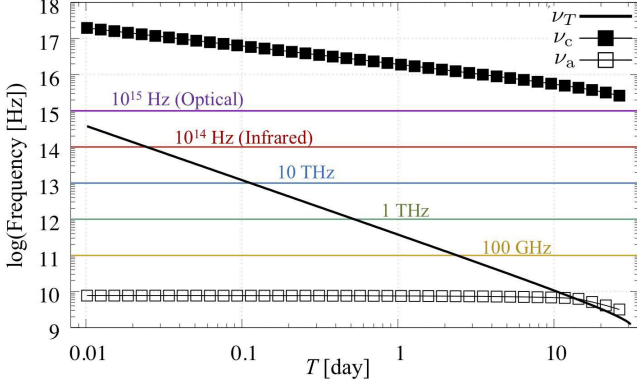


Figure 4. Temporal variations of characteristic frequencies, $\nu_T = \nu_m(\chi = y = 1)$ (black solid line), the synchrotron cooling frequency ν_c (filled squares), and the self-absorption frequency ν_a (open squares).

$R_{\perp, \max} \simeq 0.26 R_l / \gamma_l \simeq 4 \times 10^{16} (T/1 \text{ day})^{5/8} \text{ cm}$, that our treatment of averaging i', q', u' in Section 3 is justified.

The integrated flux spectrum has a broken power-law form because of the ν dependence of synchrotron power (Equation 19) at each position, and its peak frequency is given by

$$\nu_T = \nu_m(\chi = y = 1). \quad (32)$$

The image of the observed intensity tends to have a sharp ring shape for $\nu/\nu_T > 1$, while for $\nu/\nu_T < 1$, the image tends to be a slab-like shape (cf. Granot et al. 1999a, and see also Figure 6 below). Figure 4 shows ν_T (black solid line) for our parameter choice during $T = 0.01 - 30$ days. $\nu_T = \gamma_l(1 + \beta)\nu'_T$ evolves with time as $\nu_T \propto \gamma_l \gamma_m^2 B' \propto \gamma_l (\epsilon_e e' / n')^2 \sqrt{\epsilon_B e'} \propto \gamma_l^4 \propto T^{-3/2}$.

We consider the frequency range of $10^{11} - 10^{15}$ Hz, at which the synchrotron cooling and self-absorption are not important for our parameter set. Equating the synchrotron cooling timescale of a single electron with the dynamical timescale $t' = R_l / (c\gamma_l) = 16\gamma_l T$, we obtain the cooling frequency measured in the observer frame at $\chi = y = 1$ as

$$\nu_c = \gamma_l(1 + \beta_l) \frac{3q_e B'}{16m_{e,c}} \left(\frac{6\pi m_{e,c}}{\sigma_T B'^2 t'} \right)^2, \quad (33)$$

where $\beta_l = \sqrt{1 - 1/\gamma_l^2}$. In our setup, it remains at $\gtrsim 10^{15}$ Hz during $T = 0.01 - 30$ days, as displayed in Figure 4 (filled squares). The synchrotron self-absorption coefficient at $\nu' < \nu'_m$ can be estimated as (Rybicki & Lightman 1979; Granot et al. 1999b)

$$\alpha'_{\nu'} = \frac{3^{2/3} \sqrt{\pi} (p+2)(p-1)}{5\Gamma(\frac{5}{6})} \frac{q_e^{8/3}}{(m_{e,c})^{8/3}} n' B'^{2/3} \gamma_m^{-5/3} \nu'^{-5/3} \quad (34)$$

where $\Gamma(\zeta)$ is the gamma function. Then, we can estimate the absorption frequency ν_a as 0.247 times the

frequency at which $R_l \alpha'_{\nu'} / \gamma_l = 1$, where $\alpha'_{\nu'}$ is taken at $\chi = y = 1$, and the numerical factor comes from the effects of radiative transfer in the shocked fluid. We also plot ν_a in Figure 4 (open squares). It is constant for $\nu' < \nu'_m$, while $\nu_a \propto T^{-(3p+2)/2(p+4)}$ for $\nu' > \nu'_m$ (e.g. Granot & Sari 2002), and as a result, it remains at $\lesssim 10$ GHz. Hence, our calculations based on the synchrotron power formula (Equation 19) are applicable from the submillimeter band (100 GHz) to the optical band (10^{15} Hz).

5. RESULTS

We show the calculation results of synchrotron polarization from collimated blast waves as functions of T and ν mainly for the case of $\xi^2 = 0$ and their interpretation in this section. Figure 5 represents the calculated PDs,

$$\frac{Q}{I} = \frac{\int_{-\pi}^{\pi} d\phi \int_0^1 S_Q x dx}{\int_{-\pi}^{\pi} d\phi \int_0^1 S_I x dx} \quad (35)$$

for the given $\theta_v = 3$ degree, at frequencies of 10^{15} Hz (optical), 10^{14} Hz (infrared), 10 THz, 1 THz, and 100 GHz during $T = 0.01 - 30$ days (note that $U = 0$). We find that the temporal behaviors of PDs in the optical and radio bands are basically the same in the sense that the PD curves have two peaks, but the radio PD is significantly lower than the optical one with their ratio at the first PD peaks is ~ 5 . Moreover, the PDs of radio bands begin to approach that of optical band once $\nu/\nu_T \gtrsim 1$, at $T \sim 0.5$ day for 1 THz and $T \sim 3$ day for 100 GHz (see Figure 4).

Figure 6 shows the images of surface brightness S_I at the frequencies of 10^{15} Hz (optical; $\nu/\nu_T \gg 1$ case), 10 THz, and 100 GHz ($\nu/\nu_T \ll 1$ case) for the given observed times $T = 0.1, 0.4$, and 1.0 day and viewing angle $\theta_v = 3$ degree. A missing part gets larger with time in each wave band due to the finite extent of the jet and the growth of the egg size. The image shape at 10 THz is similar to that at 100 GHz at $T = 0.1$ day, but becomes similar to that at the optical band at $T = 1$ day. This behavior corresponds to that of the PD curves shown in Figure 5.

We note that even if we consider a nearby event, say at a distance ~ 100 Mpc, the angular size of its image is $\sim R_{\perp, \max} / (100 \text{ Mpc}) \sim 30(T/1 \text{ day})^{5/8} \mu\text{as}$. The imaging polarimetry of such a transient object is difficult for the current telescopes. Thus we calculate the PD curves and PD spectra by integrating the polarized flux over the image (Equation 35), while we show the (polarized) intensity images (Figure 6) just for explaining physical mechanisms. Below we will explain the details of relationship between the PD curves and the asymmetry of images.

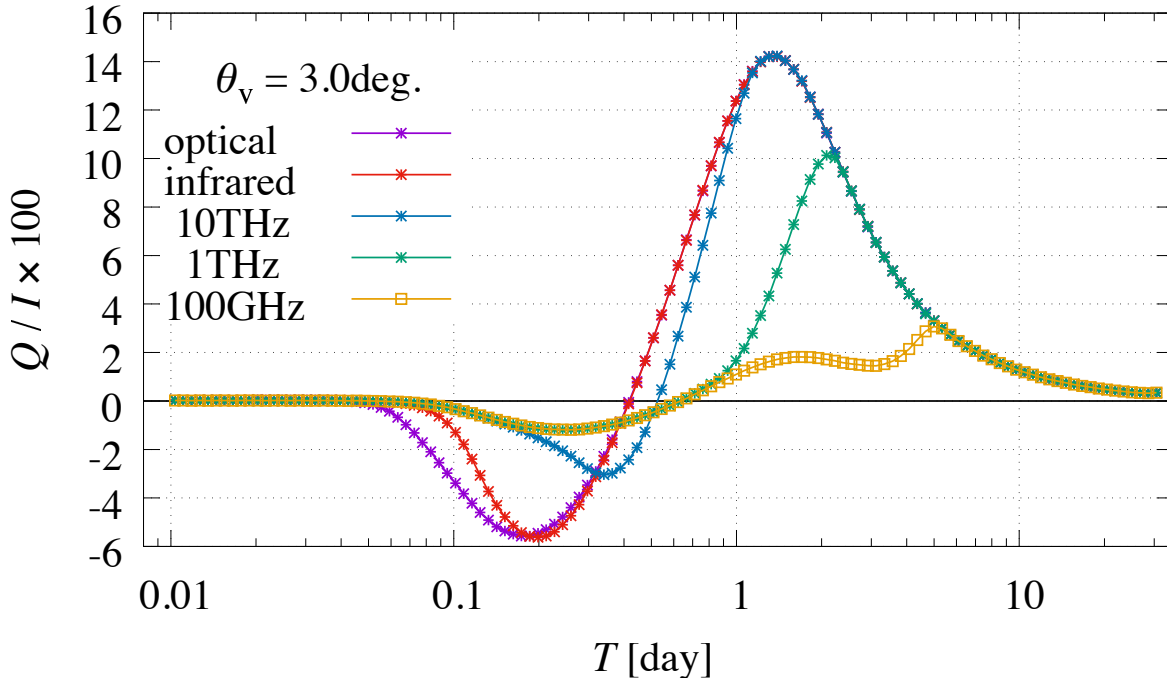


Figure 5. PD curves for $\xi^2 = 0$ and $\theta_v = 3$ degree, at frequencies 10^{15} Hz (optical), 10^{14} Hz (infrared), 10 THz, 1 THz, and 100 GHz during $T = 0.01$ -30 days. The 100 GHz PD at the initial peak is smaller than that of optical band by a factor of ~ 5 , but begins to approach the optical curve once $\nu/\nu_T \gtrsim 1$. The two curves overlap when \tilde{S}_Q/\tilde{S}_I becomes identical at the two bands (see Figure 8).

5.1. Temporal behaviors of PDs

Firstly, we review the temporal behavior of optical PD (Sari 1999; Ghisellini & Lazzati 1999; Lazzati 2006): The PD curve has two peaks, and the PA rotates by 90 degree between the two peaks. This can be understood by the temporal change of the image shown in Figure 6 (top). The shape of the optical image is always like a ring (or an asymmetric ring) because of $\nu/\nu_T \gg 1$ (Granot et al. 1999a). Figure 7 represents the flux density element $dF/dS_{\perp}dy$, which shows that the bright ring is produced by the blue region in the egg. The lines of $\cos \phi_{ec}(x, y) = 1$ (black line) and $\cos \phi_{ec}(x, y) = -1$ (white line) are also shown in the x - y plane. The region between the two white lines corresponds to $\cos \phi_{ec} < -1$ ($P' \neq 0$ for an arbitrary ϕ), that between the white and black lines to $-1 < \cos \phi_{ec} < 1$ (P' depends on ϕ), and the other region to $\cos \phi_{ec} > 1$ ($P' = 0$ for an arbitrary ϕ). From these figures we can see that at $T \lesssim 0.1$ day the optical image does not show a clear asymmetry. Figure 6 (bottom) shows that the surface polarized brightness $\sqrt{S_Q^2 + S_U^2}$ is also large on the ring. The local PA is identical to ϕ , as illustrated in Figure 2. Therefore, since we observe the emission from a GRB as a point source, the net PD is negligible due to the axisymmetry

of the local PA distribution. Then, as time goes, the optical image is asymmetric (i.e., having a missing part), and the symmetry breaking gives rise to nonzero PD. By considering the superposition of linearly polarized waves, we can see that the observed PD has one local maximum at $\phi_p \sim 3\pi/4$ (the first peak) and zero PD at $\phi_p \sim \pi/2$ (rotation of PA). The PD decays after the second maximum when most of the bright ring is missing (see more quantitative explanation in Section 5.2).

The PD curve at 100 GHz is similar to the optical PD curve until $T \sim 3$ day at which $\nu/\nu_T \sim 1$ (see Figure 4), but the peak PD is lower. Figure 6 (bottom) shows that the 100 GHz image is not ring-like because of $\nu/\nu_T \ll 1$, in contrast to the optical image. From Figure 7 we can see that a larger area with $0 < x < 1$ contributes to the observed intensity image compared to the optical case (Granot et al. 1999a). In this central part the surface polarized brightness $\sqrt{S_Q^2 + S_U^2}$ is small as can be seen in Figure 6 (bottom). Therefore, the total emission at 100 GHz has a net PD lower than that at the optical band.

The 100 GHz PD curve begins to approach the optical curve once $\nu/\nu_T \gtrsim 1$, synchronizing with the behavior of the intensity images, i.e., the image shape becomes similar to that of optical. This also explains the behav-

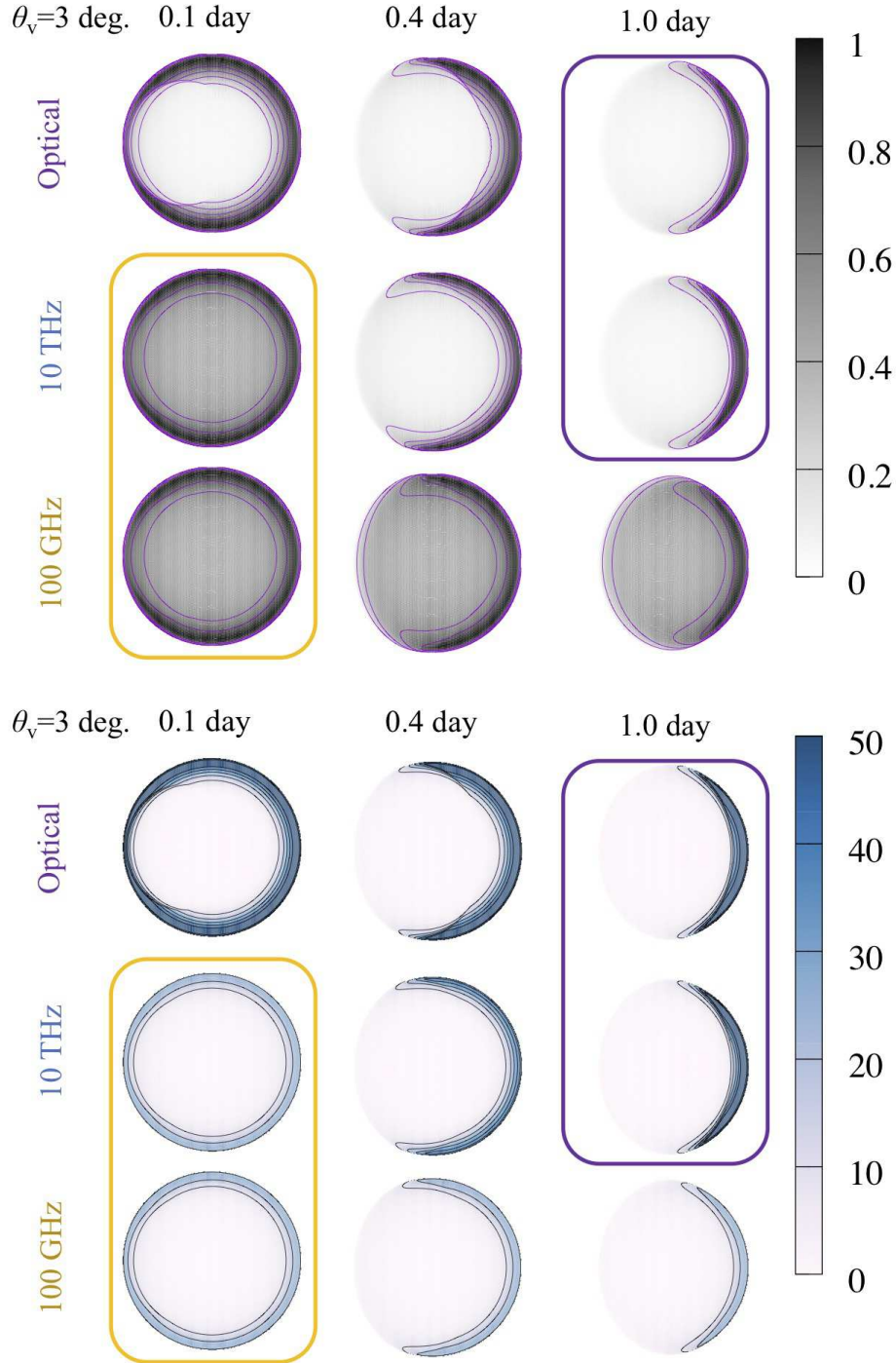


Figure 6. Surface brightness of S_I (top) and $\sqrt{S_Q^2 + S_U^2}$ (bottom) for $\nu = 10^{15}$ Hz (optical), 10 THz and 100 GHz with $\xi^2 = 0$ and $\theta_v = 3$ degree at $T = 0.1, 0.4,$ and 1.0 day. The Stokes S_I is normalized by its maximum value $S_{I,\max}$, while as for the Stokes $\sqrt{S_Q^2 + S_U^2}$, we display $\sqrt{S_Q^2 + S_U^2}/S_{I,\max} \times 100$. The image at 10 THz is almost the same as the 100 GHz image ($\nu_{100\text{GHz}}/\nu_T \ll 1$) at $T = 0.1$ day, approaches the optical image ($\nu_{\text{opt}}/\nu_T \gg 1$) at $T = 0.4$ day, and becomes almost the same as the optical image at $T = 1.0$ day.

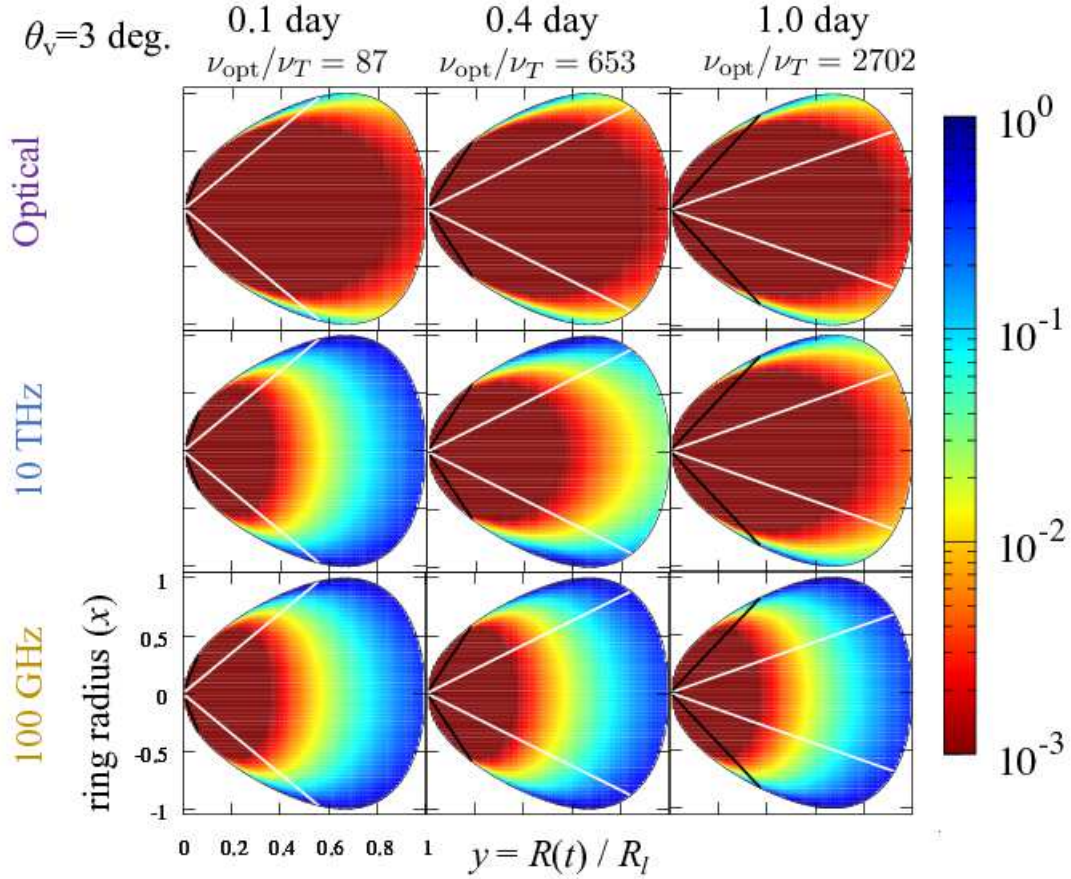


Figure 7. The flux density element $dF/dS_{\perp}dy$ (in arbitrary units) in the x - y plane for the same parameter values as for Figure 6. The black and white lines are $\cos \phi_{\text{ec}}(x, y) = 1$ and $\cos \phi_{\text{ec}}(x, y) = -1$ (white line), respectively. The region between the two white lines corresponds to $\cos \phi_{\text{ec}} < -1$ ($P' \neq 0$ for an arbitrary ϕ), between the white and black lines corresponds to $-1 < \cos \phi_{\text{ec}} < 1$ (P' depends on ϕ), and the other region corresponds to $\cos \phi_{\text{ec}} > 1$ ($P' = 0$ for an arbitrary ϕ).

iors of PD curves at the other bands (1 THz, 10 THz, and infrared). Interestingly, when ν/ν_T becomes unity after the second peak, the curves show the third peaks as a result of the approach to the optical curve.

5.2. Further Quantitative Understanding

To understand the PD curves more quantitatively, we derive analytical estimate of the PDs. First of all, as shown in Figure 2, we regard ϕ_p as a representative azimuthal angle dividing the intensity image into the region having a missing part ($-\pi \leq \phi \leq -\phi_p$ and $\phi_p \leq \phi \leq \pi$) and the rest ($-\phi_p \leq \phi \leq \phi_p$). Here, we set $\phi_p \sim \phi_{ec}(y_e)$, where $y_e = 5^{-\frac{1}{4}}$ denotes the edge of the egg $(x, y) = (1, y_e)$ ($(\chi, y) = (1, y_e)$), for simplicity, although the brightest part on $\chi = 1$ is slightly different. We define $x_e(\phi)$ as the angular distance of the outer edge of bright part from the line of sight. In the region without the missing part, x_e is always unity, while in the region with the missing part, x_e is a function of ϕ in general. Next, for the region without the missing part we define $\tilde{S}_I \equiv \int_0^1 S_I x dx$ and $\tilde{S}_Q \equiv \int_0^1 (S_Q / \cos 2\phi) x dx$, and approximate \tilde{S}_I and \tilde{S}_Q as ϕ independent by ignoring the detailed structure of the images (e.g. the optical image at $T = 0.4$ day shown in Figure 6). This approximation leads to a rough estimate of Q/I by which we can catch some essential points on the multi-wave band polarization. Then we obtain

$$\begin{aligned} I &= \int_{-\pi}^{\pi} d\phi \int_0^1 S_I x dx \\ &\sim \int_{-\phi_p}^{\phi_p} d\phi \int_0^1 S_I x dx + 2 \int_{\phi_p}^{\pi} d\phi \int_0^{x_e(\phi)} S_I x dx, \\ &\sim 2\phi_p \tilde{S}_I + 2 \int_{\phi_p}^{\pi} \Delta \tilde{S}_I d\phi, \end{aligned} \quad (36)$$

$$\begin{aligned} Q &= \int_{-\pi}^{\pi} d\phi \int_0^1 S_Q x dx \\ &\sim \int_{-\phi_p}^{\phi_p} d\phi \int_0^1 S_Q x dx + 2 \int_{\phi_p}^{\pi} d\phi \int_0^{x_e(\phi)} S_Q x dx, \\ &\sim \tilde{S}_Q \sin 2\phi_p + 2 \int_{\phi_p}^{\pi} \Delta \tilde{S}_Q \cos 2\phi d\phi, \end{aligned} \quad (37)$$

and $U = 0$. Here, we have also defined $\Delta \tilde{S}_I \equiv \int_0^{x_e(\phi)} S_I x dx$ and $\Delta \tilde{S}_Q \equiv \int_0^{x_e(\phi)} (S_Q / \cos 2\phi) x dx$ for the region with the missing part. Let us further approximate $\Delta \tilde{S}_I$ and $\Delta \tilde{S}_Q$ as ϕ independent, the observed PD is finally written as

$$\frac{Q}{I} \sim \frac{\tilde{S}_Q \sin 2\phi_p}{\tilde{S}_I} \frac{1 - \Delta \tilde{S}_Q / \tilde{S}_Q}{1 + (\pi/\phi_p - 1) \Delta \tilde{S}_I / \tilde{S}_I}. \quad (38)$$

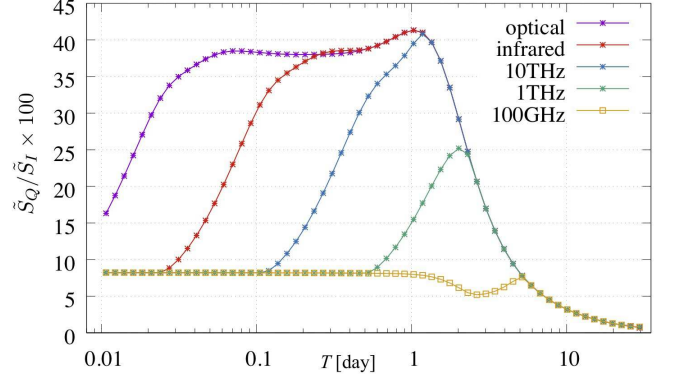


Figure 8. Temporal variation of the factor \tilde{S}_Q/\tilde{S}_I for $\phi = 0$ at the multiple wave bands for the same parameter values as Figure 5.

Since $\Delta \tilde{S}_Q/\tilde{S}_Q \ll 1$ and $\Delta \tilde{S}_I/\tilde{S}_I \lesssim 1$ (see Figure 6), the rightmost factor is around unity. The factor \tilde{S}_Q/\tilde{S}_I represents the wavelength dependence of Q/I through the wavelength dependences of the S_I and $\sqrt{S_Q^2 + S_U^2}$ images shown in Figure 6. The factor $\sin 2\phi_p/2\phi_p$ describes the cancellation of superposition of local linear polarizations for our present case of radial local PAs, and leads to the first peak PD at $\phi_p \sim 3\pi/4$ and the rotation of PA at $\phi_p \sim \pi/2$.

Figure 8 shows the calculation result of \tilde{S}_Q/\tilde{S}_I for $\phi = 0$ at the multiple wave bands for the same parameter values as Figure 5. At the optical band, $\tilde{S}_Q/\tilde{S}_I \sim \text{const.}$ for $0.1 \lesssim T \lesssim 1$ day. The decay time of \tilde{S}_Q/\tilde{S}_I ($T \sim 1$ day at optical) produces the second PD peak. This is the time at which $\theta_j + \theta_v \sim 0.6\gamma_l^{-1}$, which corresponds to the so-called jet break time T_j (e.g. Sari 1999; Ghisellini & Lazzati 1999), when most of the bright highly polarized ring emission is missing. The factor $\sin 2\phi_p/2\phi_p$ explains the behavior of the PD curve; the ratio of $\sin 2\phi_p/2\phi_p \sim -0.2$ at $\phi_p \sim 3\pi/4$ to ~ 0.4 at $\phi_p \sim \pi/3$ (at $T = T_j$) is consistent with the ratio of the first peak PD, $Q/I \simeq -6\%$, to the second peak PD, $Q/I \sim 14\%$ (Figure 5). At the other wave bands, \tilde{S}_Q/\tilde{S}_I increases once $\nu/\nu_T \gtrsim 1$, from which the PD curves begin to approach the optical PD curve, as shown in Figure 5. At the time \tilde{S}_Q/\tilde{S}_I overlaps with that of optical band, the PD curves also overlap. We can understand the difference in PD between the optical band and 100 GHz band by the difference in \tilde{S}_Q/\tilde{S}_I ; this factor is different by a factor of ~ 5 around the PD peak times, which agrees with the numerical results of PDs (e.g. the first peak PDs $Q/I \simeq -6\%$ at the optical band and $Q/I \simeq -1\%$ at 100 GHz).

5.3. PD curves for different θ_v

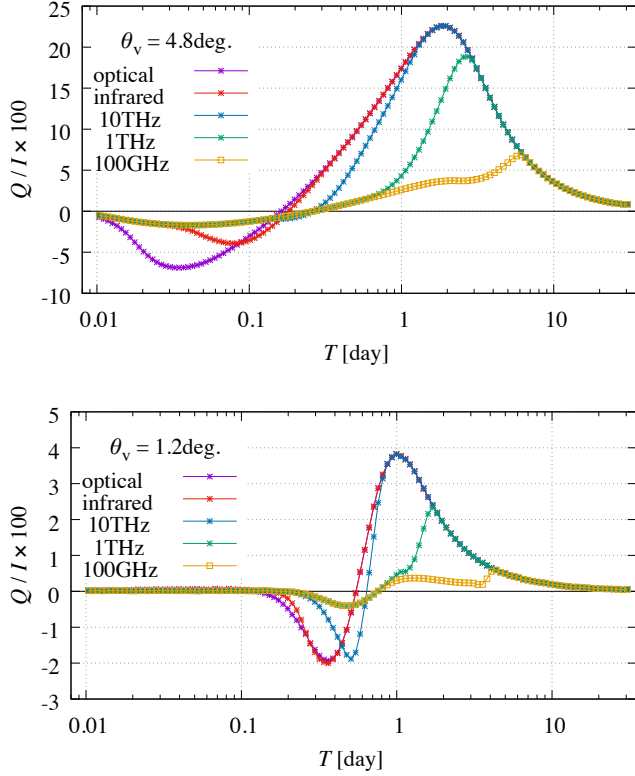


Figure 9. PD curves for $\theta_v = 4.8$ degree (top panel) and 1.2 degree (bottom panel) with the same values as the other parameters as Figure 5.

Figure 9 (top) shows the multi-wave band PD curves calculated for $\theta_v = 0.8$ degree and $\theta_j = 4.8$ degree. The overall behaviors are similar to those for $\theta_v = 3$ degree (Figure 5), but the image begins to be asymmetric earlier, and the PA flips ($\phi_p \sim \pi/2$) also occur earlier than the case of $\theta_v = 3$ degree. On the other hand, the jet break time (when $\theta_j + \theta_v \sim 0.6\gamma_l^{-1}$) is later. The value of \tilde{S}_Q/\tilde{S}_I is the same as that for $\theta_v = 3$ degree, but its decay time is $T \simeq 2$ day. Thus, the PD is determined mainly by $\sin 2\phi_p/2\phi_p$, and the later jet break time (at which $\sin 2\phi_p/2\phi_p \sim 0.6$) makes the second peak PDs higher than those for $\theta_v = 3$ degree. The ratio of the first peak PDs between the optical and 100 GHz is ~ 5 also in this case due to the same value of \tilde{S}_Q/\tilde{S}_I .

Figure 9 (bottom panel) shows the multi-waveband PD curves calculated for $\theta_v = 0.2\theta_j = 1.2$ degree. In this case the image begins to be asymmetric later and the jet break time is earlier than in the case of $\theta_v = 3$ degree. The value of \tilde{S}_Q/\tilde{S}_I also does not change also in this case, but its decay time is $T \simeq 0.6$ day. This makes the second peak PDs lower than those for $\theta_v = 3$ degree. We should note that for the optical and infrared bands, the first PD peak time of $T \sim 0.4$ day is significantly earlier than the peak time of $\sin 2\phi_p/2\phi_p$ ($T \sim 0.6$ day).

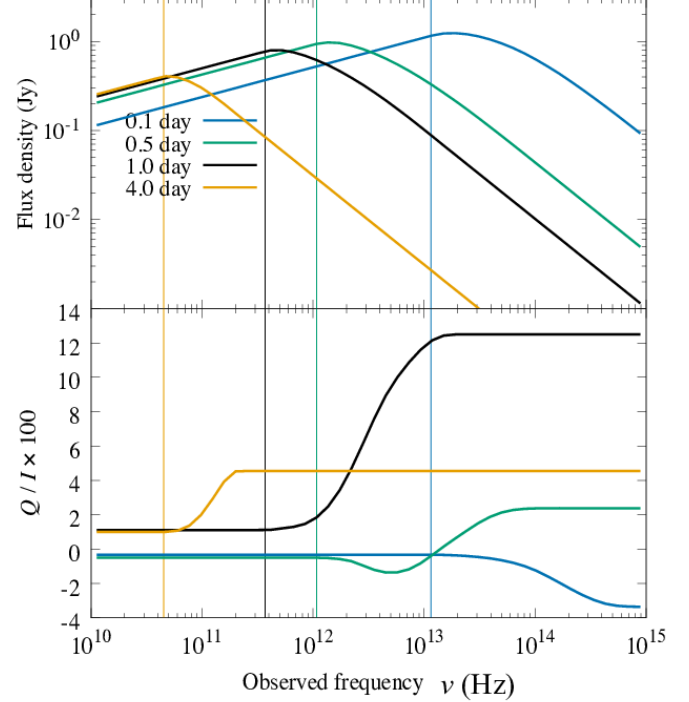


Figure 10. The top panel shows the spectra of Stokes I for $\xi^2 = 0$ and $\theta_v = 3$ degree at $T = 0.1$ (blue), 0.5 (green), 1.0 (black), and 4.0 (yellow) days. We assume a nearby GRB with a luminosity distance of $d_L = 100$ Mpc. The bottom panel shows the PDs. The vertical thin lines indicate $\nu/\nu_T = 1$ at each time.

This is mainly due to our approximation $\phi_p \sim \phi_{ec}(y_e)$ for the rough estimate of Q/I . The brightest part of $dS_{\perp}/d\chi dy$ is at $y < y_e$ (see Figure 7).

5.4. PD Spectra

Figure 10 shows spectra of the observed Stokes I and PDs for $\xi^2 = 0$ and $\theta_v = 3$ degree at $T = 0.1, 0.5, 1.0,$ and 4.0 days. Here, we consider a nearby GRB event with a luminosity distance of $d_L = 100$ Mpc. The PDs at $\nu < \nu_T$ are always lower than that at optical bands ($\nu \gg \nu_T$) because of the difference in \tilde{S}_Q/\tilde{S}_I . The PA at 100 GHz is the same as that at the optical band at most of the times as shown by the PD spectra at $T = 0.1$ and 1.0 days, but they can be different by 90 degrees as shown by the PD spectrum at $T = 0.5$ day within a short time period. This period is $T \sim 0.4 - 0.7$ day as indicated by the PD curves (Figure 5). These are characteristic properties of the plasma-scale turbulent magnetic field model, so that simultaneous polarimetric observations at the optical and radio bands would provide a firm test of this model. In other words, if the PDs at the radio bands of $\nu < \nu_T$ are higher than that at the optical band or the difference in PAs at the two bands

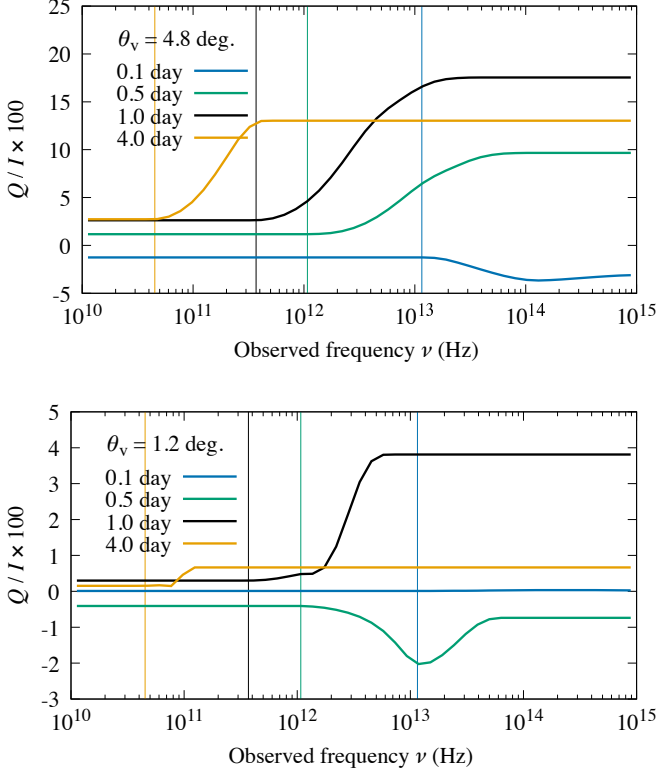


Figure 11. The PD spectra for $\theta_v = 4.8$ degree (top panel) and 1.2 degree (bottom) panel. The vertical thin lines indicate $\nu/\nu_T = 1$ at $T = 0.1$ (blue), 0.5 (green), 1.0 (black), and 4.0 (yellow) days.

is not 0 or 90 degree, we can rule out the plasma-scale turbulent field model.

The PD spectra are flat at $\nu < \nu_T$ (low PD regime) and $\nu > \nu_B$ (high PD regime), while the PD gradually varies at $\nu_T < \nu < \nu_B$, with $\nu_B \sim 40\nu_T$ at $T < T_j$. This behavior can be explained by the variation of \tilde{S}_I/\tilde{S}_Q in terms of ν with fixed T (see Figure 8). At $T > T_j$, ν_B/ν_T rapidly decreases (e.g. $\nu_B/\nu_T \sim 5$ at $T = 4.0$ day). The ratio ν_B/ν_T at $T < T_j$ does not significantly depend on θ_v because of the same value of \tilde{S}_Q/\tilde{S}_I . We should note, however, that the detailed shapes of PD spectra are not explained only by the wavelength dependence of \tilde{S}_Q/\tilde{S}_I . For example, at $T = 0.1$ day the PD at infrared band (10^{14} Hz) is much lower than that of the optical band, but the \tilde{S}_Q/\tilde{S}_I of infrared band is already comparable to that of the optical band. In such cases, the differences in PDs are affected by the third factor in Eq. (38) or more accurately by the combination of the flux density element $dF_\nu/dS_\perp dy$ profile and $\cos \phi_{ec}$.

Figure 11 represents the PD spectra for $\theta_v = 4.8$ degree (top panel) and $\theta_v = 1.2$ degree (bottom panel). The spectra are also flat at $\nu < \nu_T$ and $\nu > \nu_B$. At $\nu_T < \nu < \nu_B$, the curves are different from the case

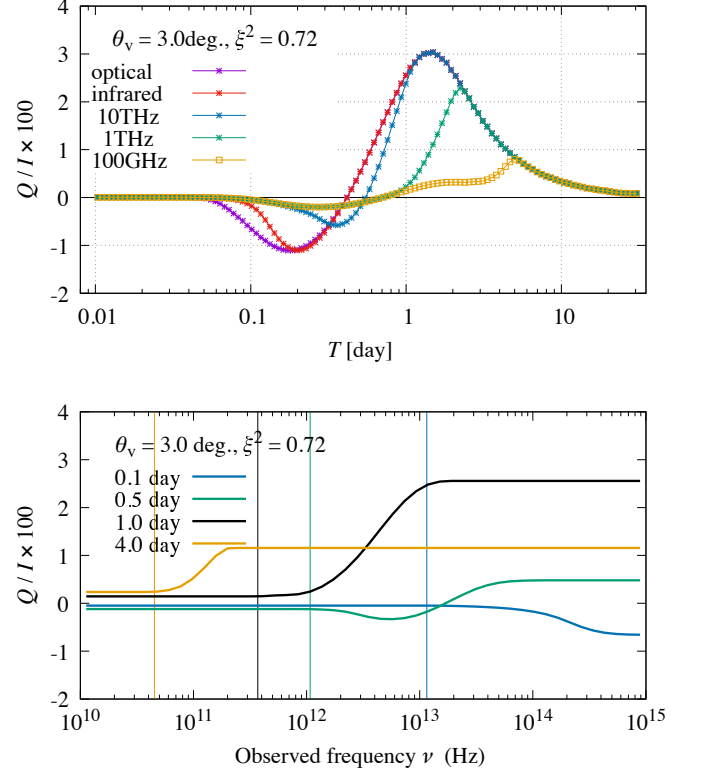


Figure 12. The top panel is the PD curves for $\xi^2 = 0.72$ and $\theta_v = 3$ degree. The bottom panel is the PD spectra at $T = 0.1$ (blue), 0.5 (green), 1.0 (black), and 4.0 (yellow) days. The vertical thin lines indicate $\nu/\nu_T = 1$ at each time.

of $\theta_v = 3.0$ degree. This is due to the difference in times at which the images begin to be asymmetric (see Section 5.3).

5.5. PD curves and spectra for $\xi^2 = 0.72$

We also calculate the PD curves and spectra for $\xi^2 = 2\langle B_\parallel^2 \rangle / \langle B_\perp^2 \rangle = 0.72$ and $\theta_v = \theta_j/2 = 3$ degree. The results are shown in Figure 12. The less anisotropic magnetic field structure leads to a smaller $\langle f \rangle$ (see Figure 3) and weaker net PDs. The value of $\xi^2 = 0.72$ reproduces the observed typical late-phase optical PD $\sim 1 - 3\%$. The ratio of PD peak values in the optical and radio bands is ~ 10 . The temporal behaviors of multi-band intensity image shapes are almost the same as the case of $\xi^2 = 0$, which provide almost the same times of PD peaks and PA 90° changes and values of ν_B .

6. SUMMARY AND DISCUSSION

We have studied multi-wave band polarization of GRB afterglows under the assumption of an anisotropic plasma-scale turbulent magnetic field and an optically thin limit by using the standard calculation formulae of

relativistic blast wave dynamics and synchrotron emission. We have clarified that since GRB afterglows are observed as point sources, the net linear polarizations are determined by the image shape intensity which depends on the observed frequency and its asymmetry due to the collimation of outflow (see Figure 6). Our calculation results have shown that the PD at $\nu < \nu_T$ is always lower than the optical PD (Figures 5 and 10), since the region with low polarized intensity in the image is larger at $\nu < \nu_T$, i.e., \tilde{S}_Q/\tilde{S}_I is smaller at $\nu < \nu_T$ (see Figure 6 and 8). We find that the PD gradually varies above $\nu \sim \nu_T$, and the break frequency of the high PD regime to the low one is $\nu_B \sim 40\nu_T$ at $T < T_j$, while ν_B/ν_T rapidly decreases at $T > T_j$ (Figure 10). We also show that the difference in PAs between the high and low PD regimes is zero or 90 degrees. Thus, the simultaneous polarimetric observations of late-phase GRB afterglows at the radio (typically $\nu < \nu_B$) and optical bands (typically $\nu > \nu_B$) would be a new determinative test of the anisotropic plasma-scale turbulent magnetic field model.

Radio polarizations have been measured recently for GRB 171205A (Urata et al. 2019) and GRB 190114C (Laskar et al. 2019) with ALMA at the frequency of $\nu_{\text{ALMA}} \simeq 97.5$ GHz, which is typically higher than the synchrotron self-absorption frequency. For GRB 171205A, the polarization of forward shock emission was measured as PD $\simeq 0.27 \pm 0.04$ %. This is significantly lower than the typical optical PD of late-phase afterglows of $\sim 1 - 3$ % (Covino et al. 2004). The observed intensity light curve and spectrum indicate $\nu_T \sim 150$ GHz and $T \sim 2.5T_j$ at the polarization measurement (Urata et al. 2019), so that we find $\nu_{\text{ALMA}} < \nu_B$. These observational indications appear consistent with the anisotropic plasma-scale turbulent field model (although we have no simultaneous optical polarization measurement for this GRB). However, the observed PAs seem to vary in the range of 90.5 – 104.5 GHz, which are at odds with the model. Interestingly, for GRB 190114C, the radio polarimetric observations performed for the reverse shock emission show gradual temporal change of PA, which rules out the plasma-scale turbulent field model (Laskar et al. 2019).

The magnetic field structure of GRB forward shock blast waves has been examined by using only optical polarimetric data so far (Covino & Gotz 2016). The temporal PA flips by 90 degrees, predicted by the plasma-scale field model, were observed in some GRBs such as GRB 091018 and GRB 121024A (Wiersema et al. 2014) while not observed in some other GRBs such as GRB 020813 (Lazzati et al. 2004). Here, we should note that the temporal PA flips are not necessarily observed for jets with angular structure (Rossi et al.

2004) and for the shocked region including ordered field (Granot & Königl 2003). The angular structure of GRB jets may be constrained by modeling the densely observed intensity light curves, as performed for short GRB 170817A with the detection of the gravitational wave of the progenitor system (e.g. Gill & Granot 2020; Takahashi & Ioka 2019). The afterglow of GRB 091208B observed by the Kanata telescope at $T = 149 - 706$ s appears to be from the forward shock and has a PD of 10.4 ± 2.5 %. Such a high PD at the early phase does not favor the plasma-scale turbulent field model (Uehara et al. 2012).

The magnetic field in the blast waves may not be dominated by the turbulent component on the plasma skin-depth scale but by that on the hydrodynamic scale (Sironi & Goodman 2007; Inoue et al. 2013b; Duffell & MacFadyen 2014; Tomita et al. 2019). Such field structure is suggested in observed non- (or sub-) relativistically expanding blast waves, for example, Tycho’s supernova remnant (Shimoda et al. 2018) and AT2018cow (Huang et al. 2019). Especially for the former example, a Kolmogorov scaling is seen in the magnetic field energy spectrum. The differences between the optical and radio polarizations in this field structure should be clarified in separate papers. Probably the temporal variation (or the distribution in the egg) of the field coherence scale may be crucial.

Furthermore, for the hydrodynamic-scale magnetic field case, the Faraday rotation effects within the shocked region should be taken into account. If only a fraction f_e of the electrons swept by the shock are energized to form the nonthermal energy spectrum at $\gamma_e \geq \gamma_m \sim \Gamma \epsilon_e m_p/m_e$, the Faraday depolarization by non-energized thermal electrons at $\gamma_e \sim \Gamma$ may suppress the PD even at $\nu > \nu_a$ (in the ALMA band, Toma et al. 2008; Urata et al. 2019) and the PAs may be a complex function of ν (Sokoloff et al. 1998). In the case of $f_e < 1$, E_{iso} should be $1/f_e$ times larger than the ordinary estimates under the assumption of $f_e = 1$ (Eichler & Waxman 2005). While some particle-in-cell simulations suggest $f_e \simeq 1$ (Sironi & Spitkovsky 2011; Kumar et al. 2015), it should be confirmed by observations (see also Ressler & Laskar 2017; Warren et al. 2018; Asano et al. 2020). Simultaneous polarimetric observations of GRB afterglows at the optical and multiple radio bands with ALMA and more theoretical investigations offer the potential power for understanding the magnetic field structure and the electron energy distribution in the downstream of relativistic collisionless shocks.

ACKNOWLEDGMENTS

We thank J. Matsumoto, S. Tomita, Y. Urata, and A. Kuwata for useful discussions. This work is partly supported by JSPS Grants-in-Aid for Scientific Research No. 18H01245 (KT) and No. 20J01086 (JS).

REFERENCES

- Abbott, B. P., Abbott, R., Abbott, T. D., et al. 2017, *ApJL*, 848, L13, doi: [10.3847/2041-8213/aa920c](https://doi.org/10.3847/2041-8213/aa920c)
- Asano, K., Murase, K., & Toma, K. 2020, arXiv e-prints, arXiv:2007.06307. <https://arxiv.org/abs/2007.06307>
- Blandford, R. D., & McKee, C. F. 1976, *Physics of Fluids*, 19, 1130, doi: [10.1063/1.861619](https://doi.org/10.1063/1.861619)
- Burgess, J. M., Kole, M., Berlato, F., et al. 2019, *A&A*, 627, A105, doi: [10.1051/0004-6361/201935056](https://doi.org/10.1051/0004-6361/201935056)
- Coburn, W., & Boggs, S. E. 2003, *Nature*, 423, 415, doi: [10.1038/nature01612](https://doi.org/10.1038/nature01612)
- Covino, S., Ghisellini, G., Lazzati, D., & Malesani, D. 2004, *Astronomical Society of the Pacific Conference Series*, Vol. 312, *Polarization of Gamma-Ray Burst Optical and Near-Infrared Afterglows*, ed. M. Feroci, F. Frontera, N. Masetti, & L. Piro, 169
- Covino, S., & Gotz, D. 2016, *Astronomical and Astrophysical Transactions*, 29, 205. <https://arxiv.org/abs/1605.03588>
- Duffell, P. C., & MacFadyen, A. I. 2014, *ApJL*, 791, L1, doi: [10.1088/2041-8205/791/1/L1](https://doi.org/10.1088/2041-8205/791/1/L1)
- Eichler, D., & Waxman, E. 2005, *ApJ*, 627, 861, doi: [10.1086/430596](https://doi.org/10.1086/430596)
- Ghisellini, G., & Lazzati, D. 1999, *MNRAS*, 309, L7, doi: [10.1046/j.1365-8711.1999.03025.x](https://doi.org/10.1046/j.1365-8711.1999.03025.x)
- Gill, R., & Granot, J. 2020, *MNRAS*, 491, 5815, doi: [10.1093/mnras/stz3340](https://doi.org/10.1093/mnras/stz3340)
- Götz, D., Covino, S., Fernández-Soto, A., Laurent, P., & Bošnjak, Ž. 2013, *MNRAS*, 431, 3550, doi: [10.1093/mnras/stt439](https://doi.org/10.1093/mnras/stt439)
- Götz, D., Laurent, P., Lebrun, F., Daigne, F., & Bošnjak, Ž. 2009, *ApJL*, 695, L208, doi: [10.1088/0004-637X/695/2/L208](https://doi.org/10.1088/0004-637X/695/2/L208)
- Granot, J., & Königl, A. 2003, *ApJL*, 594, L83, doi: [10.1086/378733](https://doi.org/10.1086/378733)
- Granot, J., Piran, T., & Sari, R. 1999a, *ApJ*, 513, 679, doi: [10.1086/306884](https://doi.org/10.1086/306884)
- . 1999b, *ApJ*, 527, 236, doi: [10.1086/308052](https://doi.org/10.1086/308052)
- Granot, J., & Sari, R. 2002, *ApJ*, 568, 820, doi: [10.1086/338966](https://doi.org/10.1086/338966)
- Granot, J., & Taylor, G. B. 2005, *ApJ*, 625, 263, doi: [10.1086/429536](https://doi.org/10.1086/429536)
- Granot, J., & van der Horst, A. J. 2014, *PASA*, 31, e008, doi: [10.1017/pasa.2013.44](https://doi.org/10.1017/pasa.2013.44)
- Gruzinov, A., & Waxman, E. 1999, *ApJ*, 511, 852, doi: [10.1086/306720](https://doi.org/10.1086/306720)
- Hjorth, J., & Bloom, J. S. 2012, *The Gamma-Ray Burst - Supernova Connection*, 169–190
- Huang, K., Shimoda, J., Urata, Y., et al. 2019, *ApJL*, 878, L25, doi: [10.3847/2041-8213/ab23fd](https://doi.org/10.3847/2041-8213/ab23fd)
- Inoue, S., Granot, J., O’Brien, P. T., et al. 2013a, *Astroparticle Physics*, 43, 252, doi: [10.1016/j.astropartphys.2013.01.004](https://doi.org/10.1016/j.astropartphys.2013.01.004)
- Inoue, T., Shimoda, J., Ohira, Y., & Yamazaki, R. 2013b, *ApJL*, 772, L20, doi: [10.1088/2041-8205/772/2/L20](https://doi.org/10.1088/2041-8205/772/2/L20)
- Jordana-Mitjans, N., Mundell, C. G., Kobayashi, S., et al. 2020, *ApJ*, 892, 97, doi: [10.3847/1538-4357/ab7248](https://doi.org/10.3847/1538-4357/ab7248)
- Kalemci, E., Boggs, S. E., Kouveliotou, C., Finger, M., & Baring, M. G. 2007, *ApJS*, 169, 75, doi: [10.1086/510676](https://doi.org/10.1086/510676)
- Kato, T. N. 2005, *Physics of Plasmas*, 12, 080705, doi: [10.1063/1.2017942](https://doi.org/10.1063/1.2017942)
- Keshet, U., Katz, B., Spitkovsky, A., & Waxman, E. 2009, *ApJL*, 693, L127, doi: [10.1088/0004-637X/693/2/L127](https://doi.org/10.1088/0004-637X/693/2/L127)
- Kimura, S. S., Murase, K., Mészáros, P., & Kiuchi, K. 2017, *ApJL*, 848, L4, doi: [10.3847/2041-8213/aa8d14](https://doi.org/10.3847/2041-8213/aa8d14)
- Kole, M. 2019, in *International Cosmic Ray Conference*, Vol. 36, *36th International Cosmic Ray Conference (ICRC2019)*, 572
- Kopač, D., Mundell, C. G., Japelj, J., et al. 2015, *ApJ*, 813, 1, doi: [10.1088/0004-637X/813/1/1](https://doi.org/10.1088/0004-637X/813/1/1)
- Kumar, P., & Zhang, B. 2015, *PhR*, 561, 1, doi: [10.1016/j.physrep.2014.09.008](https://doi.org/10.1016/j.physrep.2014.09.008)
- Kumar, R., Eichler, D., & Gedalin, M. 2015, *ApJ*, 806, 165, doi: [10.1088/0004-637X/806/2/165](https://doi.org/10.1088/0004-637X/806/2/165)
- Lan, M.-X., Wu, X.-F., & Dai, Z.-G. 2018, *ApJ*, 860, 44, doi: [10.3847/1538-4357/aac26e](https://doi.org/10.3847/1538-4357/aac26e)
- Laskar, T., Hull, C. L. H., & Cortes, P. 2020, arXiv e-prints, arXiv:2004.06730. <https://arxiv.org/abs/2004.06730>
- Laskar, T., Alexander, K. D., Gill, R., et al. 2019, *ApJL*, 878, L26, doi: [10.3847/2041-8213/ab2247](https://doi.org/10.3847/2041-8213/ab2247)
- Lazzati, D. 2006, *New Journal of Physics*, 8, 131, doi: [10.1088/1367-2630/8/8/131](https://doi.org/10.1088/1367-2630/8/8/131)

- Lazzati, D., Covino, S., Gorosabel, J., et al. 2004, *A&A*, 422, 121, doi: [10.1051/0004-6361:20035951](https://doi.org/10.1051/0004-6361:20035951)
- Mao, J., & Wang, J. 2017, *ApJ*, 838, 78, doi: [10.3847/1538-4357/aa6628](https://doi.org/10.3847/1538-4357/aa6628)
- Matsumiya, M., & Ioka, K. 2003, *ApJL*, 595, L25, doi: [10.1086/378879](https://doi.org/10.1086/378879)
- Medvedev, M. V., & Loeb, A. 1999, *ApJ*, 526, 697, doi: [10.1086/308038](https://doi.org/10.1086/308038)
- Mészáros, P. 2002, *ARA&A*, 40, 137, doi: [10.1146/annurev.astro.40.060401.093821](https://doi.org/10.1146/annurev.astro.40.060401.093821)
- Mundell, C. G., Kopač, D., Arnold, D. M., et al. 2013, *Nature*, 504, 119, doi: [10.1038/nature12814](https://doi.org/10.1038/nature12814)
- Murase, K., Ioka, K., Nagataki, S., & Nakamura, T. 2006, *ApJL*, 651, L5, doi: [10.1086/509323](https://doi.org/10.1086/509323)
- Nishikawa, K. I., Hardee, P., Richardson, G., et al. 2003, *ApJ*, 595, 555, doi: [10.1086/377260](https://doi.org/10.1086/377260)
- Panaitescu, A., & Kumar, P. 2002, *ApJ*, 571, 779, doi: [10.1086/340094](https://doi.org/10.1086/340094)
- Piran, T. 2004, *Reviews of Modern Physics*, 76, 1143, doi: [10.1103/RevModPhys.76.1143](https://doi.org/10.1103/RevModPhys.76.1143)
- Rees, M. J. 1966, *Nature*, 211, 468, doi: [10.1038/211468a0](https://doi.org/10.1038/211468a0)
- Ressler, S. M., & Laskar, T. 2017, *ApJ*, 845, 150, doi: [10.3847/1538-4357/aa8268](https://doi.org/10.3847/1538-4357/aa8268)
- Rossi, E. M., Lazzati, D., Salmonson, J. D., & Ghisellini, G. 2004, *MNRAS*, 354, 86, doi: [10.1111/j.1365-2966.2004.08165.x](https://doi.org/10.1111/j.1365-2966.2004.08165.x)
- Rutledge, R. E., & Fox, D. B. 2004, *MNRAS*, 350, 1288, doi: [10.1111/j.1365-2966.2004.07665.x](https://doi.org/10.1111/j.1365-2966.2004.07665.x)
- Rybicki, G. B., & Lightman, A. P. 1979, *Radiative processes in astrophysics*
- Sagiv, A., Waxman, E., & Loeb, A. 2004, *ApJ*, 615, 366, doi: [10.1086/423977](https://doi.org/10.1086/423977)
- Sari, R. 1999, *ApJL*, 524, L43, doi: [10.1086/312294](https://doi.org/10.1086/312294)
- Sharma, V., Iyyani, S., Bhattacharya, D., et al. 2019, *ApJL*, 882, L10, doi: [10.3847/2041-8213/ab3a48](https://doi.org/10.3847/2041-8213/ab3a48)
- Shimoda, J., Akahori, T., Lazarian, A., Inoue, T., & Fujita, Y. 2018, *MNRAS*, 480, 2200, doi: [10.1093/mnras/sty2034](https://doi.org/10.1093/mnras/sty2034)
- Sironi, L., & Goodman, J. 2007, *ApJ*, 671, 1858, doi: [10.1086/523636](https://doi.org/10.1086/523636)
- Sironi, L., Keshet, U., & Lemoine, M. 2015, *SSRv*, 191, 519, doi: [10.1007/s11214-015-0181-8](https://doi.org/10.1007/s11214-015-0181-8)
- Sironi, L., & Spitkovsky, A. 2011, *ApJ*, 726, 75, doi: [10.1088/0004-637X/726/2/75](https://doi.org/10.1088/0004-637X/726/2/75)
- Sironi, L., Spitkovsky, A., & Arons, J. 2013, *ApJ*, 771, 54, doi: [10.1088/0004-637X/771/1/54](https://doi.org/10.1088/0004-637X/771/1/54)
- Sokoloff, D. D., Bykov, A. A., Shukurov, A., et al. 1998, *MNRAS*, 299, 189, doi: [10.1046/j.1365-8711.1998.01782.x](https://doi.org/10.1046/j.1365-8711.1998.01782.x)
- Spitkovsky, A. 2008, *ApJL*, 682, L5, doi: [10.1086/590248](https://doi.org/10.1086/590248)
- Steele, I. A., Kopač, D., Arnold, D. M., et al. 2017, *ApJ*, 843, 143, doi: [10.3847/1538-4357/aa79a2](https://doi.org/10.3847/1538-4357/aa79a2)
- Stringer, E., & Lazzati, D. 2020, *ApJ*, 892, 131, doi: [10.3847/1538-4357/ab76d2](https://doi.org/10.3847/1538-4357/ab76d2)
- Takahashi, K., & Ioka, K. 2019, arXiv e-prints, arXiv:1912.01871. <https://arxiv.org/abs/1912.01871>
- Taylor, G. B., Momjian, E., Pihlström, Y., Ghosh, T., & Salter, C. 2005, *ApJ*, 622, 986, doi: [10.1086/428346](https://doi.org/10.1086/428346)
- Toma, K. 2013, arXiv e-prints, arXiv:1308.5733. <https://arxiv.org/abs/1308.5733>
- Toma, K., Ioka, K., & Nakamura, T. 2008, *ApJL*, 673, L123, doi: [10.1086/528740](https://doi.org/10.1086/528740)
- Toma, K., Yoon, S.-C., & Bromm, V. 2016, *SSRv*, 202, 159, doi: [10.1007/s11214-016-0250-7](https://doi.org/10.1007/s11214-016-0250-7)
- Toma, K., Sakamoto, T., Zhang, B., et al. 2009, *ApJ*, 698, 1042, doi: [10.1088/0004-637X/698/2/1042](https://doi.org/10.1088/0004-637X/698/2/1042)
- Tomita, S., Ohira, Y., & Yamazaki, R. 2019, *ApJ*, 886, 54, doi: [10.3847/1538-4357/ab4a10](https://doi.org/10.3847/1538-4357/ab4a10)
- Troja, E., Lipunov, V. M., Mundell, C. G., et al. 2017, *Nature*, 547, 425, doi: [10.1038/nature23289](https://doi.org/10.1038/nature23289)
- Uehara, T., Toma, K., Kawabata, K. S., et al. 2012, *ApJL*, 752, L6, doi: [10.1088/2041-8205/752/1/L6](https://doi.org/10.1088/2041-8205/752/1/L6)
- Urata, Y., Toma, K., Huang, K., et al. 2019, *ApJL*, 884, L58, doi: [10.3847/2041-8213/ab48f3](https://doi.org/10.3847/2041-8213/ab48f3)
- van der Horst, A. J., Paragi, Z., de Bruyn, A. G., et al. 2014, *MNRAS*, 444, 3151, doi: [10.1093/mnras/stu1664](https://doi.org/10.1093/mnras/stu1664)
- van Eerten, H. J., & MacFadyen, A. I. 2012, *ApJ*, 751, 155, doi: [10.1088/0004-637X/751/2/155](https://doi.org/10.1088/0004-637X/751/2/155)
- Warren, D. C., Barkov, M. V., Ito, H., Nagataki, S., & Laskar, T. 2018, *MNRAS*, 480, 4060, doi: [10.1093/mnras/sty2138](https://doi.org/10.1093/mnras/sty2138)
- Wiersema, K., Covino, S., Toma, K., et al. 2014, *Nature*, 509, 201, doi: [10.1038/nature13237](https://doi.org/10.1038/nature13237)
- Wigger, C., Hajdas, W., Arzner, K., Güdel, M., & Zehnder, A. 2004, *ApJ*, 613, 1088, doi: [10.1086/423163](https://doi.org/10.1086/423163)
- Yonetoku, D., Murakami, T., Gunji, S., et al. 2011, *ApJL*, 743, L30, doi: [10.1088/2041-8205/743/2/L30](https://doi.org/10.1088/2041-8205/743/2/L30)
- . 2012, *ApJL*, 758, L1, doi: [10.1088/2041-8205/758/1/L1](https://doi.org/10.1088/2041-8205/758/1/L1)
- Zhang, S.-N., Kole, M., Bao, T.-W., et al. 2019, *Nature Astronomy*, 3, 258, doi: [10.1038/s41550-018-0664-0](https://doi.org/10.1038/s41550-018-0664-0)
- Zhang, W., & MacFadyen, A. 2009, *ApJ*, 698, 1261, doi: [10.1088/0004-637X/698/2/1261](https://doi.org/10.1088/0004-637X/698/2/1261)